nature nanotechnology

LETTERS

https://doi.org/10.1038/s41565-018-0117-z

2D matrix engineering for homogeneous quantum dot coupling in photovoltaic solids

Jixian Xu[1], Oleksandr Voznyy[1], Mengxia Liu[1], Ahmad R. Kirmani[2], Grant Walters[1], Rahim Munir[2], Maged Abdelsamie[2], Andrew H. Proppe[1,3], Amrita Sarkar[4], F. Pelayo García de Arquer[1], Mingyang Wei[1], Bin Sun[1], Min Liu[1,5], Olivier Ouellette[1], Rafael Quintero-Bermudez[1], Jie Li[1], James Fan[1], Lina Quan[1], Petar Todorovic[1], Hairen Tan[1], Sjoerd Hoogland[1], Shana O. Kelley[3,6], Morgan Stefik[4], Aram Amassian[2]* and Edward H. Sargent[1]*

Colloidal quantum dots (CQDs) are promising photovoltaic (PV) materials because of their widely tunable absorption spectrum controlled by nanocrystal size[1,2]. Their bandgap tunability allows not only the optimization of single-junction cells, but also the fabrication of multijunction cells that complement perovskites and silicon[3]. Advances in surface passivation[2,4–7], combined with advances in device structures[8], have contributed to certified power conversion efficiencies (PCEs) that rose to 11% in 2016[9]. Further gains in performance are available if the thickness of the devices can be increased to maximize the light harvesting at a high fill factor (FF). However, at present the active layer thickness is limited to ~300 nm by the concomitant photocarrier diffusion length. To date, CQD devices thicker than this typically exhibit decreases in short-circuit current (J_{SC}) and open-circuit voltage (V_{OC}), as seen in previous reports[3,9–11]. Here, we report a matrix engineering strategy for CQD solids that significantly enhances the photocarrier diffusion length. We find that a hybrid inorganic–amine coordinating complex enables us to generate a high-quality two-dimensionally (2D) confined inorganic matrix that programmes internanoparticle spacing at the atomic scale. This strategy enables the reduction of structural and energetic disorder in the solid and concurrent improvements in the CQD packing density and uniformity. Consequently, planar devices with a nearly doubled active layer thicknesses (~600 nm) and record values of J_{SC} (32 mA cm^{-2}) are fabricated. The V_{OC} improved as the current was increased. We demonstrate CQD solar cells with a certified record efficiency of 12%.

In recent studies, composition-matching matrices have been explored as a solder between CQDs to improve carrier mobility[12]. Lattice-matching matrices, such as perovskites, have been shown to improve the efficiency of CQD luminescence[13]. We reasoned that the limited photocarrier diffusion length and V_{OC} deficit could arise from spatial variations in the nanostructure of the matrix throughout a CQD PV film (Fig. 1). Photocarrier transport between CQDs is sensitive to the thickness of the interstitial matrix, at the atomic scale, from the perspective both of electronic tunnelling and of resonance energy transfer[1,12–15]. Detrimental inhomogeneity in the matrix (such as CQD overcoupling due to surface fusion in the absence of matrix or CQD over isolation due to matrix accumulations) increases structural and energetic disorder and degrades the diffusion length in the film as well as the devices' V_{OC} (Fig. 1d)[3,10,14–17].

Rutherford backscattering spectroscopy (RBS) studies of previously reported best-performing PbS CQD PV solids[9] reveal a matrix component that includes stoichiometric PbI_2 in surprisingly high amounts, ~40–50% relative to PbS (Fig. 1b and Supplementary Fig. 1). This agrees with the amount required for a full monolayer coverage on the surfaces of the PbS CQDs (bandgap ~1.3 eV and diameter ~3 nm). We believed that the conditions under which such matrices are formed during film solidification could benefit from further attention.

Therefore, we pursued the goal to increase the photocarrier diffusion length in CQD PV solids via matrix improvements (Fig. 1c,e). We would do so by limiting the PbI_2 matrix component to be a 2D material, a strategy enabled by developing a PbI_2–hybrid-amine coordinating complex that forms in a manner analogous to the materials synthesis of 2D perovskites[18,19] (Fig. 1c). The strategy promotes the growth of the PbI_2 matrix into a thin configuration with single-atom layers. We sought a 2D strategy to prevent the formation of thick (multiple-atom layers) regions of matrix that could otherwise form during film solidification.

We investigated PbI_2–hybrid-amine coordinating complexes, initially by ultraviolet–visible–near-infrared ((UV–vis–NIR) absorption spectroscopy (Fig. 2a). We compared PbI_2 films prepared from dimethylformamide (DMF) (the aprotic polar solvent used for CQD solution exchange), pure *N*-butylamine (BTA) (the control solvent used in the best previously published CQD PVs[9]) and the hybrid-amine mixtures (BTA and hexylamine (Methods gives the details)). A strong excitonic absorption peak ($\lambda \approx 500$ nm) was found in the hybrid-amine PbI_2 films. This feature was much less significant in the BTA case (Supplementary Fig. 2) and was not detectable in the DMF case. We associate the excitonic feature with quantum-confined layered structures observed in previous studies: layered 2D PbI_2–organic hybrid perovskites[18,19]. This notion is further confirmed by photoluminescence (PL) studies (Fig. 2b). The

[1]Department of Electrical and Computer Engineering, University of Toronto, Toronto, Ontario, Canada. [2]King Abdullah University of Science and Technology (KAUST), KAUST Solar Center (KSC), and Physical Sciences and Engineering Division, Thuwal, Saudi Arabia. [3]Department of Chemistry, University of Toronto, Toronto, Ontario, Canada. [4]Department of Chemistry and Biochemistry, University of South Carolina, Columbia, SC, USA. [5]Institute of Super-microstructure and Ultrafast Process in Advanced Materials, School of Physics and Electronics, Central South University, Changsha, Hunan, China. [6]Department of Pharmaceutical Sciences, Leslie Dan Faculty of Pharmacy, University of Toronto, Toronto, Ontario, Canada. *e-mail: aram.amassian@kaust.edu.sa; ted.sargent@utoronto.ca

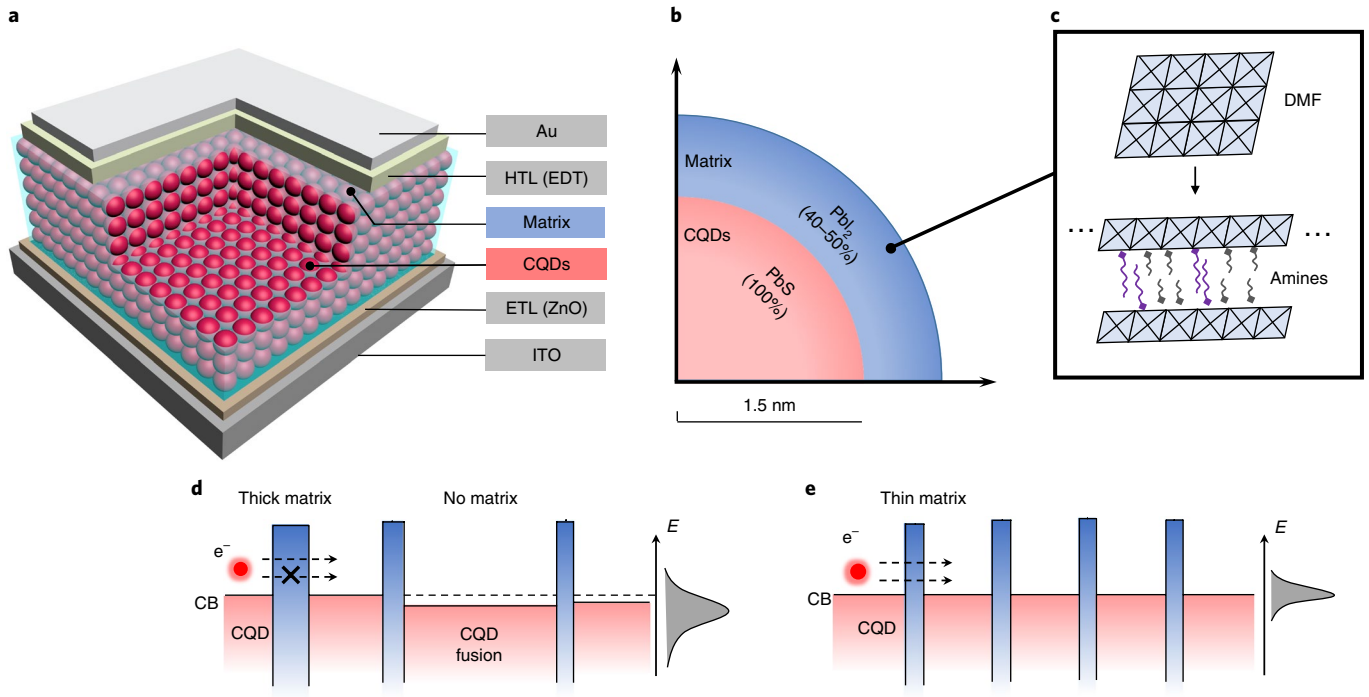

Fig. 1 | Engineering the microscopic nature of the matrix to increase the ordering and photocarrier diffusion length in CQD solids for solar cells. **a**, Schematic diagram of the effective medium model of the CQD absorber in a solar cell, where CQDs (red) assemble in a matrix medium (blue). **b**, In published best-performing PbS CQD PV solids, the matrix component is PbI_2 and its amount is ~40–50% compared with PbS in a molecular ratio, enough to account for the formation of a full monolayer coverage on the surfaces of the PbS CQDs (bandgap ~1.3 eV and diameter ~3 nm). **c**, DMF and hybrid amines are used to functionalize the PbI_2 matrix component and tailor the matrix's microstructure and distribution during the reorganization that occurs when the CQDs are solidified from solution. The PbI_2–hybrid-amine coordinating complex has a self-confined 2D layered structure that greatly suppresses inhomogeneity of the matrix due to a random 3D growth in DMF. **d**, Inhomogeneity of the matrix increases the structural and energetic disorder and reduces the diffusion length and V_{OC}. CQD over isolation due to local matrix agglomeration will block the carrier transport. CQD overcoupling due to surface fusion caused by the absence of the matrix tends to increase the V_{OC} deficit. **e**, Confining the matrix dimensionality between the CQDs and improving its homogeneity throughout the film increases the photocarrier diffusion length and reduces the V_{OC} deficit. HTL; hole-transport layer; EDT; 1,2-ethanedithiol; ETL, electron-transport layer; ITO, indium tin oxide; CB, conduction band; *E*, energy.

sharp and asymmetric PL emission (peak $\lambda \approx 520$ nm, full-width at half-maximum ~16 nm) of hybrid-amine films is a signature of the independent and substantially homogeneous population of PbI_2 monolayers. Such PL features have typically been observed in layered 2D perovskite single crystals[18] and layered PbI_2 single crystals under cryogenic conditions[20]. The emission spectra for BTA films are much broader and darker (Supplementary Fig. 2). We ascribe this to the presence of less self-similar and/or less-confined layered structures. In contrast, the random 3D growth habit of DMF films yields negligible emission, due to the numerous defects at the grain surfaces and the mutual quenching effect[20,21].

We noticed that the PL linewidth (~16 nm) of the PbI_2–hybrid-amine films is comparable to that of 2D perovskite single crystals (~16 nm) and is superior to that of 2D perovskite films (>40 nm (Supplementary Fig. 3)). This near-single-crystalline feature motivated crystallographic measurements that employed grazing incidence wide-angle X-ray scattering (GIWAXS). Conventional DMF films exhibited no detectable layered features (Fig. 2c). By contrast, sharp and discrete Bragg spots along the q_z axis were observed in hybrid-amine films (Fig. 2d and Supplementary Fig. 4), which reveals a high-quality 2D monolayer structure with long-range ordering and orientation. This finding indicated the potential to enhance the 2D confinement of the PbI_2 matrix component by leveraging the hybrid-amine coordination.

We used Fourier transform infrared (FTIR) spectroscopy to gain a further mechanistic understanding of the PbI_2–amine complex in CQD films (Fig. 2c). First, the coordination effect of amines on PbI_2 is confirmed by the consistent shift of the N–H stretch mode (3,170 cm^{-1}) and N–H scissor mode (1,560 cm^{-1}) in PbI_2–amine complexes compared with those in reference solvents of the amines (Supplementary Fig. 4)[22]. This signature of 2D PbI_2–amine complexes is present identically both in PbI_2 films and in PbI_2-capped CQD films prepared using amines (Fig. 2e and Supplementary Figs. 5 and 6c). Moreover, when the matrix-to-CQD ratio is tuned, the spectral signature of the 2D PbI_2–amine complex in CQD films is retained in the FTIR measurements (Supplementary Fig. 7d). Its lattice pattern was also identified using GIWAXS (Supplementary Fig. 7b). In contrast, such features are absent both in PbI_2 films and in CQD films prepared using DMF (Fig. 2e and Supplementary Figs. 6f and 7h). This comparison indicates that the mechanism for CQD surface functionalization is inherited from the PbI_2–amine 2D coordination in the matrix, rather than from the PbS CQD bare surfaces.

The signatures of the PbI_2–hybrid-amine complexes shown in the CQD films are consistent with those presented in pure 2D layered perovskite films[18]. This, again, indicates a confined monolayer configuration for the PbI_2 matrix stabilized by the hybrid-amine ligands, consistent with conclusions drawn from absorption spectra, PL signals and GIWAXS patterns (Fig. 2a–d). Overall, the photophysics and crystallography studies reveal a reduction of the dimensionality during the PbI_2 crystallization process associated with the incorporation of longer amines. These open up opportunities to suppress CQD fusion and the formation of thicker PbI_2 regions between CQDs. Consistent with this view, the hybrid-amine devices exhibited V_{OC} values higher than those of the best control devices made using BTA and DMF inks (Supplementary Fig. 8).

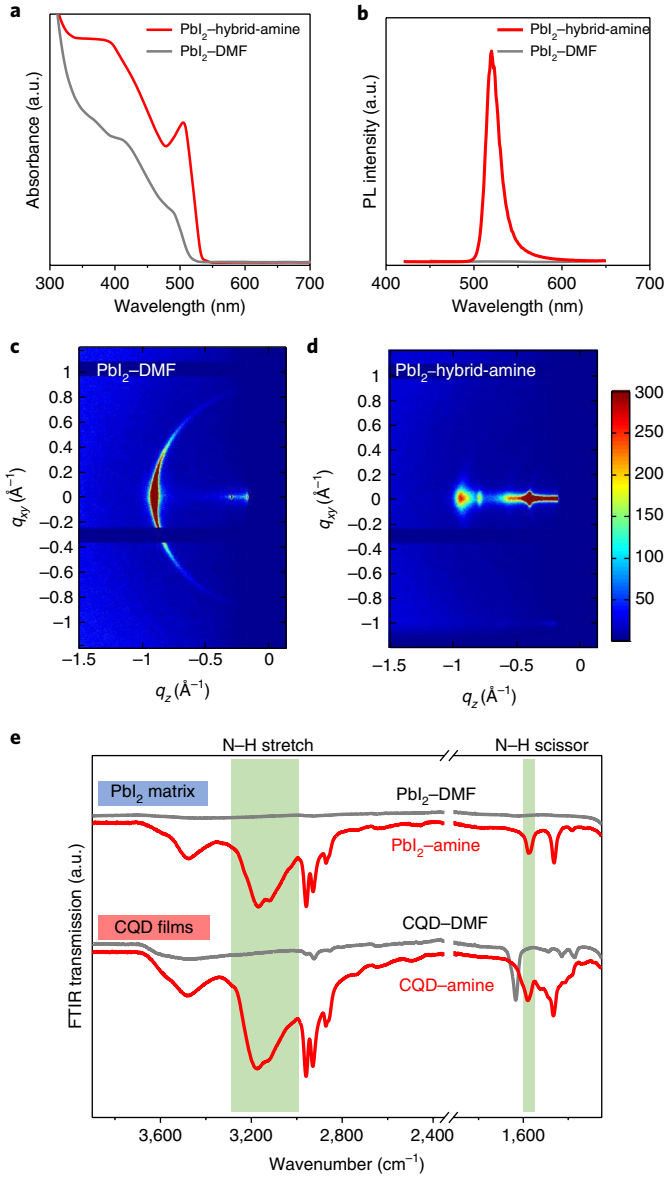

Fig. 2 | Enhanced 2D confinement in the matrix of CQD solids. a, UV–vis–NIR absorption curves of PbI_2 deposited from hybrid amines (red) and DMF (dark grey). Hybrid-amine films show a strong excitonic feature located at the band edge (~500 nm), which results from the quantum-confinement effect in layered configurations of PbI_2–hybrid-amine coordinating complexes. DMF films show no excitonic feature. **b**, Room-temperature PL of PbI_2 deposited from the hybrid amines (red) and DMF (dark grey). Hybrid-amine films show a narrow and asymmetric PL peak. DMF films show no PL features. **c**,**d**, GIWAXS patterns for PbI_2 deposited from DMF (**c**) and PbI_2 deposited from hybrid amines (**d**). The PbI_2–hybrid-amine complex shows a near-single-crystalline pattern of a 2D monolayer structure in parallel with the substrate. **e**, ATR-FTIR spectroscopy of the PbI_2–amine coordinating complex signatures in the N–H stretch modes (green band at ~3,200 cm^{-1}) and N–H scissor modes (green band at ~1,590 cm^{-1}). The PbI_2 films and CQD films deposited using hybrid amines (red) show consistent signatures for the PbI_2–amine coordinating complexes. PbI_2 films and CQD films deposited using DMF (grey) show no signatures of the PbI_2–amine coordinating complexes. a.u., arbitrary units.

The PbI_2–hybrid-amine matrix leads to CQD inks with an improved colloidal stability (Supplementary Fig. 9) that benefit from the enhanced steric repulsion[23,24] of the longer amine surfactants (hexylamine). We also observed narrower PL peaks and higher PL quantum yields from hybrid-amine inks (Supplementary Fig. 10), which indicate high-quality surfaces stabilized in the solution phase. We propose that, compared with control BTA inks, this new matrix mediates a less-disruptive CQD-densification process during the transition from the solution to the solid phase. In this regard, in situ spectroscopic ellipsometry, absorption and thermogravimetric analyses were used to study the evolution of the CQD film thickness, absorption and mass, respectively, during the postannealing (Supplementary Fig. 11). We found that 40–50% increases in film density occur, and these are associated with remarkable reductions of film thickness and the amount of volatile amine species. These changes are quantitatively much more appreciable than the near-imperceptible changes of the control BTA CQD films subjected to the same postannealing conditions. After the postannealing process, hybrid-amine films are PV-quality films. This sol–gel-like solidification process of the PbI_2–hybrid-amine matrix is reminiscent of sol–gel solidification processes reported in lead halide perovskites[25,26].

In the resultant CQD films, an enhanced packing density and uniformity, and therefore a reduced structural disorder, were also indicated in a suite of microscopic studies (Fig. 3). Ex situ force–indentation curves measured with an atomic force microscope (AFM) were used to study differences in the mechanical characteristics of CQD films that stemmed from different traits of the matrix materials. In agreement with observations from the in situ studies, the hybrid-amine films without postannealing are characteristically soft, and feature much lower elastic moduli and larger hysteresis in the force–height response compared to control BTA films (Supplementary Fig. 12). After CQD rearrangement and densification during postannealing, the hybrid-amine films exhibited concurrent improvements (~20%) of the elastic modulus and hysteresis compared with the control BTA films (Fig. 3a,b). In addition, tapping-mode topographic AFM analysis of the film morphology showed that the local and global smoothness can be greatly improved by using hybrid-amine inks (Fig. 3c and Supplementary Fig. 13). For the progressively increasing field of views (5×5 to 30×30 μm^2), hybrid-amine films retain a surface roughness of ~0.6 nm, whereas control BTA films' roughness increases from 1.4 nm to ~2 nm (Fig. 3d). The enhanced elastic modulus, in conjunction with improved smoothness, implies a simultaneous optimization of the CQD packing density and uniformity. Enhanced packing uniformity has recently been recognized as greatly benefitting the carrier transport in CQD assemblies[1,9,14,16,27,28].

Further analysis using grazing-incidence small-angle X-ray scattering (GISAXS) confirmed the structural enhancement both in density and uniformity[29]. The localized diffraction pattern indicates the orientational in-plane ordering of CQDs in hybrid-amine films (Fig. 3e and Supplementary Fig. 6b). This feature is absent in CQD films prepared using DMF (Supplementary Fig. 6e). Compared with control BTA films (Supplementary Fig. 10), we can clearly identify an additional ~10% densification in the planar direction and an average ~6–7% densification of the interdot spacing from azimuthal integration[30] of the diffraction pattern (Fig. 3f). The enhanced densification is also shown in observations that hybrid-amine films produced with a postannealing process have narrower diffraction peaks compared with those of control BTA films without any postannealing. The peak is ~20% narrower (from 0.69 nm^{-1} to 0.51 nm^{-1}), a result of the greatly enhanced packing uniformity.

The CQD packing density in the control BTA films was previously characterized as being the densest compared with other state-of-art PV-quality films (for example, tetrabutylammonium halide salt-exchanged CQD films and metal–halide perovskite-exchanged CQD films)[9]. Attempts to densify the BTA films further with annealing typically deteriorated the V_{OC} (Supplementary Figs. 8 and 14), a finding we attributed to the increased inhomo-

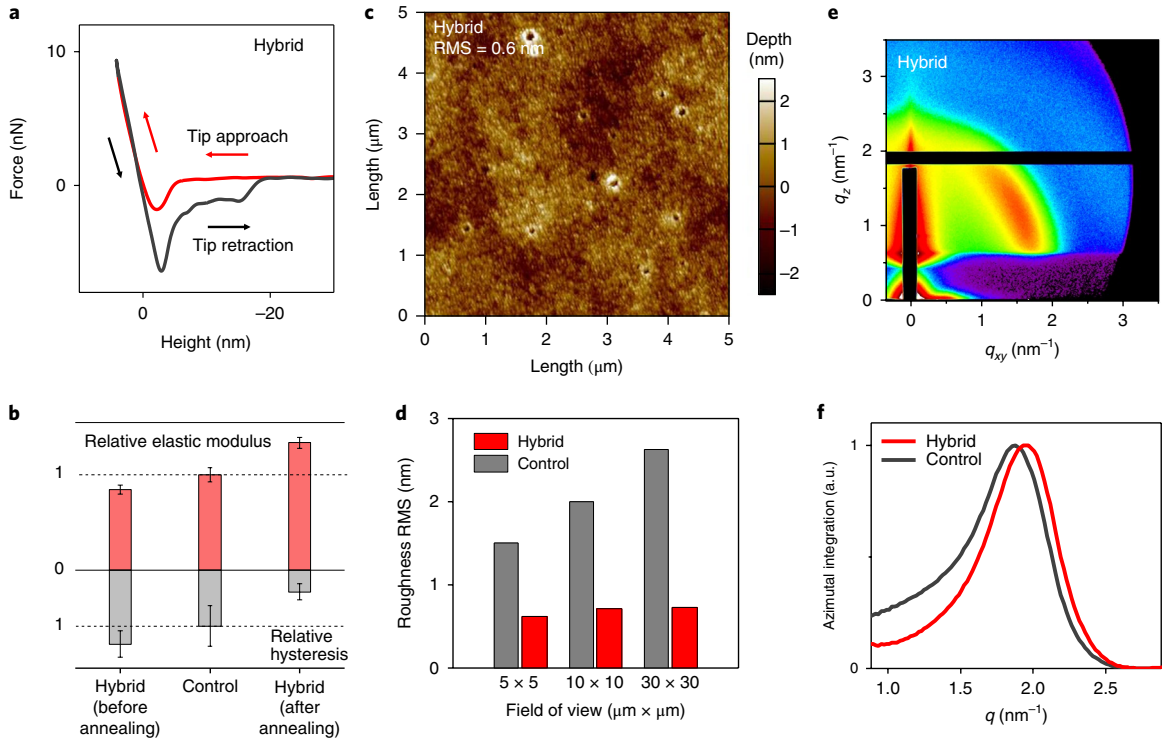

Fig. 3 | Enhanced packing density and uniformity, and reduced structural disorder in CQD solids for solar cells. a, Mechanical characteristics of hybrid-amine films (force–indentation curves) measured by an AFM. Arrows indicate the tip approach and retraction. **b**, Elastic moduli and plastic deformation (calculated from the slope and its hysteresis in the linear rising region of force–indentation curves) between hybrid-amine films (before and after postannealing) and best-performing control films. Postannealed hybrid-amine films are PV-quality films and are characterized in **c**–**f**. **c**, Topographic AFM morphology analysis of hybrid-amine films, which show a surface roughness (RMS) of ~0.6 nm. **d**, Over progressively increasing field of views (5 × 5 to 30 × 30 μm^2), the hybrid-amine films (red) exhibit a greatly reduced roughness compared with the best control films (grey). **e**, The GISAXS 2D pattern of the hybrid-amine films. The vertical black line on the lower left is the beam stop and the horizontal black line is due to the Pilatus 200k detector. The localized diffraction peak indicates the orientational in-plane ordering of the CQD assembly. **f**, Azimuthally integrated intensities of the diffraction peak. They show the distribution of interdot *d* spacing ($d \approx 1/q$) in the CQD assembly. The hybrid films (red) exhibit a ~10% reduction in planar *d* spacings, ~7% reduction in directional-average *d* spacings and peaks narrower by ~20% compared with control films (grey), which suggests the concurrently enhanced packing density and homogeneity of CQDs.

geneity from behaviour such as CQD surface fusions[3,10,14,17]. The enhanced resistance to heterogeneous fusion during CQD densification suggests that the CQD surface is greatly preserved with the aid of PbI_2–hybrid-amine complexes.

This preservation of CQD surfaces is supported by an investigation of the energetic disordering in films (Fig. 4). As observed in PL studies (Fig. 4a), additional postannealing induces a visible redshift and broadening of the peak for the best control BTA films, which indicates degradation of the energetic ordering. In contrast, in the hybrid-amine films subjected to the same postdensification process, the PL features were retained (Supplementary Fig. 15) and exhibited a sharper and slightly blueshifted PL peak relative to that of BTA films, which corresponds to an increased energetic ordering[14,17,29]. In agreement with the above film-level studies, we also characterized the energetic disordering at the device level by high-dynamic-range external quantum efficiency (HDR-EQE) measurements[9] in the energetic range of the band tail (Fig. 4b). In agreement with the PL results, the band tails of devices using hybrid-amine films are steeper than those of the best control BTA devices, and BTA films subjected to postannealing failed to preserve the band-tail sharpness.

Encouragingly, the suppression of structural and energetic disordering in the denser CQD films successfully enhances the J_{SC} and V_{OC} simultaneously in the CQD PV devices (Supplementary Fig. 14), which overcomes a long-lasting compromise that has been the focus of many previously attempted strategies[9–11,17].

In addition to the structural and energetic analyses, we also directly characterized the electronic parameters to quantify the enhancements to the photocarrier diffusion length for the optimized matrix. In the standard field effect transistor (FET) spectroscopy analysis[31], the hybrid-amine films exhibit higher n-type electronic mobility, associated with a sharper slope in the I_{DS}–V_{GS} (DS, drain to source; GS, gate to source) response (Fig. 4c). From FET subthreshold slope state density spectroscopy (Supplementary Fig. 16), hybrid-amine films also showed a reduction in sub-bandgap state densities (6.3×10^{15} cm^{-3}) by one order of magnitude compared with the best BTA control films (5.7×10^{16} cm^{-3}).

We also conducted an analysis under contact-free and photoactivated conditions. We employed the donor–acceptor scheme[32] in which a small portion of smaller-bandgap CQDs was evenly distributed in films to accept photocarriers and quench the PL emission from donor CQDs (Fig. 4d and Supplementary Fig. 17). Free charge carriers dominate the photophysical dynamics in these thick and highly coupled CQD films (Supplementary Fig. 18), a fact we attribute to rapid exciton dissociation[14,33]. Acceptor emission contributed from exciton diffusion and trion recombination[34,35] is negligible due to low inclusion ratio (<0.1%) in films and low excitation intensity (<1 Sun). The PL ratio (PL emission intensity of acceptors over that of donors in a film) increases when there are more acceptors included, for a shorter diffusion distance is required for carriers to reach the acceptors. The enhancement of mobility in hybrid-amine films is quantitatively confirmed by a twofold increase in the slope of the PL

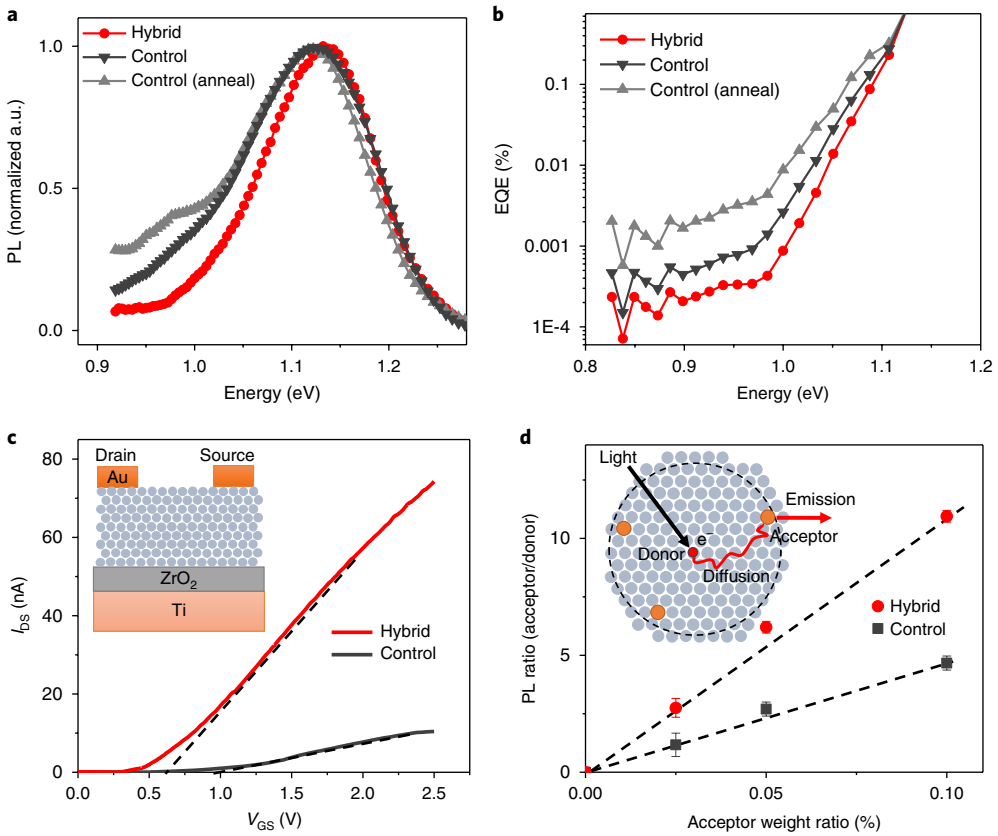

Fig. 4 | Reduced energetic disorder and enhanced electronic transport in CQD solids. a, The PL of hybrid-amine films (red circles) is sharper and slightly bluer than best-performing control films (dark grey inverted triangles). The control films densified via a postannealing process, the same as that used for hybrid-amine films, exhibit a lower-energy and broader PL (light grey triangles) than that of the nonannealed control films. **b**, The HDR-EQE of devices using hybrid-amine solids (red circles) is sharpest compared with best-performing control devices (dark grey inverted triangles) and devices that used annealed control films (light grey triangles), which represents reduced concentrations and depths of band-tail states. **c**, Transfer characteristics of FETs using control and hybrid-amine CQD films (red) and best-performing control CQD films (dark grey). The sharper slope of the current–voltage (*I*–*V*) curve indicates a higher electronic mobility. Inset: FET device structure. **d**, Transfer characteristics of photoactived carriers in donor–acceptor films that use the hybrid-amine CQDs (red) and control CQDs (dark grey). A sharper slope in the PL ratio (acceptor over the donor) curve indicates a higher mobility and longer diffusion length for the photocarriers. Inset: photocarrier dynamics in donor–acceptor films.

ratio (Fig. 4d). We further show that, at the same time as the excellent electronic transport is achieved, a prolonged excited-state lifetime is observed in transient absorption (TA) measurements (Methods and Supplementary Fig. 19). The combination of enhanced carrier transport and lifetime associated with reduced trapping defines a longer diffusion length in the hybrid-amine CQD solids.

The advantages of hybrid-amine CQD solids enable the realization of thickened PV devices that offer to enhance simultaneously the J_{SC} and V_{OC}. When we increased the absorber thickness from 250 nm to 600 nm, the full-spectrum EQE exhibited progressive broadband enhancement (Fig. 5a), with excitonic peak values of ~80% and integrated J_{SC} densities that approached 32 mA cm^{-2}, a record level in a high-efficiency CQD PV. The retained high flat response in the blue region (<800 nm) and red excitonic region (>900 nm) in 600 nm thick films indicates a collection efficiency free of degradation for photocarriers at both the front and rear contacts, respectively. The experimentally acquired internal quantum efficiencies (Supplementary Fig. 20) are spectrally flat over the absorption region and indicate a near-unity charge generation and collection efficiency within these thick planar devices. They rule out energy-dependent charge generation and also argue against a strong quantitative influence of hot exciton or carrier effects.

The J_{SC} of devices with different thicknesses, measured under standard AM 1.5G solar illumination conditions (Fig. 5b), agree quantitatively with the EQE measurements. No sign of J_{SC} saturation appeared when the absorber thickness was increased from 250 nm to 600 nm. In contrast, the devices using the best-published control films showed an optimal J_{SC} (~27 mA cm^{-2}) and PCE (~11%) at the optimal thickness of ~350 nm (Fig. 5c). In agreement with previous reports, control devices with thicker absorbers exhibited losses in V_{OC} (from 0.62 V to 0.6 V) and FF, which we attribute to insufficient carrier diffusion lengths[9,11].

The optimal devices using hybrid-amine CQD solids (excitonic peak at ~950 nm in a synthetic solution) can be achieved with thicknesses of ~500 nm. The devices showed a reproducible high performance with a champion PCE = 12.48% (Fig. 5d). One of our devices measured by an accredited PV laboratory (Newport Technology and Application Center, PV Lab) was found to display very similar figures of merit (V_{OC} = 0.647 ± 0.009 V, J_{SC} = 29.04 ± 0.60 mA cm^{-2}, FF = 63.8 ± 1.3%) with PCE = 12.01 ± 0.26% (Fig. 5d and Supplementary Fig. 21), the highest certified PCE reported for a CQD solar cell. This further verified the stability and reproducibility of our new strategy of matrix engineering.

We also demonstrate large-area (1.1 cm^{-2}) devices (Supplementary Fig. 22). The spatial and electrical uniformity of CQD films are verified by an excellent agreement among the EQE spectra measured at different locations across the large-area devices. The large-area devices exhibited *V*oc and *J*sc values that agree well with those of

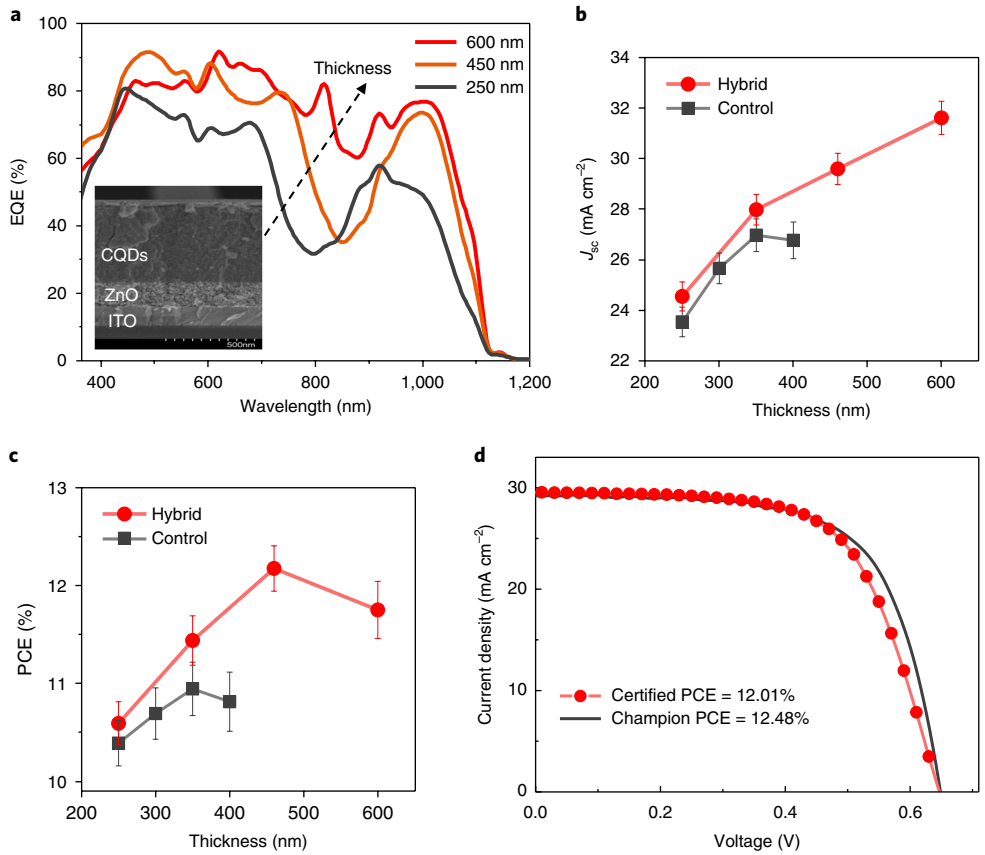

Fig. 5 | Enhanced solar cell performance in thick CQD absorbers that result from increased photocarrier diffusion lengths. a, The full-spectrum EQE increased continuously when the thickness of the absorber, prepared from a hybrid-amine ink, was increased from 250 nm to 600 nm. Inset: the cross-sectional scanning electron microscopy image of a representative device structure. **b**, Comparison of J_{SC} dependence on absorber thickness between the hybrid-amine device (red curve) and best-performing control device (grey curve). J_{SC} in the control device saturates when the thickness exceeds 350 nm. J_{SC} in the hybrid amine device keeps rising when the thickness reaches 600 nm. The devices were tested under AM1.5G 100 mW cm^{-2} illumination conditions. **c**, The comparison of absorber-thickness-dependent PCE between different types of device. The optimal thickness of the best control devices (grey curve) is ~350 nm. The optimal thickness of the hybrid-amine devices (red curve) is in the range of ~500 nm. The champion PCE of the hybrid-amine device is 12.48%. **d**, *J*–*V* curve of a certified device that exhibits a PCE of 12.01%, the highest ever reported. Statistics for each type of device are calculated using 12 samples fabricated in the same batch.

small-area (0.049 cm^{-2}) devices. The somewhat lower PCE in large-area devices relative to small-area devices majorly resides in the FF due to the limited series resistance (R_{se}) of the transparent conductive oxide. We believe that strategies such as integrating metal grids onto indium tin oxide (ITO) can reduce the R_{se} limit in large-area CQD devices.

The evolution of device performance with progressively increasing matrix-to-CQD ratios (Supplementary Fig. 23) reveals the sensitivity with respect to the matrix size. The reduced $Jsc \times FF$ associated with the thicker matrix indicates the loss of interdot carrier hopping or tunnelling. This observation supports the type-I band alignment between CQD and the matrix composition in our films (Fig. 1e).

Overall, this work showcases a matrix engineering strategy that allows significant improvements in the photocarrier diffusion length in CQD solids. The enhanced structural and energetic ordering in densified CQD films allows us to overcome the long-lasting compromise between devices' V_{OC} and J_{SC}, and therefore fulfill the advantage of building a thick device with record performance. More broadly, this study reveals the hidden sensitivity and flexibility of matrices' microscopic nature in CQD solids, and provides a means to tune material properties within the wide scope of CQD applications, such as printable devices, tandem cells, photodetectors and light-emitting diodes.

Methods

Methods, including statements of data availability and any associated accession codes and references, are available at https://doi.org/10.1038/s41565-018-0117-z.

Received: 28 July 2017; Accepted: 14 March 2018;
Published online: 23 April 2018

References

1. Kagan, C. R., Lifshitz, E., Sargent, E. H. & Talapin, D. V. Building devices from colloidal quantum dots. *Science* **353**, aac5523 (2016).
2. Luther, J. M. et al. Schottky solar cells based on colloidal nanocrystal films. *Nano Lett.* **8**, 3488–3492 (2008).
3. Ip, A. H. et al. Infrared colloidal quantum dot photovoltaics via coupling enhancement and agglomeration suppression. *ACS Nano* **9**, 8833–8842 (2015).
4. Ip, A. H. et al. Hybrid passivated colloidal quantum dot solids. *Nat. Nanotech.* **7**, 577–582 (2012).
5. Tang, J. et al. Colloidal-quantum-dot photovoltaics using atomic-ligand passivation. *Nat. Mater.* **10**, 765–771 (2011).
6. Ning, Z. et al. Air-stable n-type colloidal quantum dot solids. *Nat. Mater.* **13**, 822–828 (2014).
7. Dirin, D. N. et al. Lead halide perovskites and other metal halide complexes as inorganic capping ligands for colloidal nanocrystals. *J. Am. Chem. Soc.* **136**, 6550–6553 (2014).
8. Chuang, C.-H. M., Brown, P. R., Bulović, V. & Bawendi, M. G. Improved performance and stability in quantum dot solar cells through band alignment engineering. *Nat. Mater.* **13**, 796–801 (2014).

9. Liu, M. et al. Hybrid organic–inorganic inks flatten the energy landscape in colloidal quantum dot solids. *Nat. Mater.* **16**, 258–263 (2016).
10. Carey, G. H., Levina, L., Comin, R., Voznyy, O. & Sargent, E. H. Record charge carrier diffusion length in colloidal quantum dot solids via mutual dot-to-dot surface passivation. *Adv. Mater.* **27**, 3325–3330 (2015).
11. Lan, X. et al. 10.6% certified colloidal quantum dot solar cells via solvent-polarity-engineered halide passivation. *Nano Lett.* **16**, 4630–4634 (2016).
12. Dolzhnikov, D. S. et al. Composition-matched molecular 'solders' for semiconductors. *Science* **347**, 425–428 (2015).
13. Ning, Z. et al. Quantum-dot-in-perovskite solids. *Nature* **523**, 324–328 (2015).
14. Gilmore, R. H., Lee, E. M. Y., Weidman, M. C., Willard, A. P. & Tisdale, W. A. Charge carrier hopping dynamics in homogeneously broadened PbS quantum dot solids. *Nano Lett.* **17**, 893–901 (2017).
15. Guyot-Sionnest, P. Electrical transport in colloidal quantum dot films. *J. Phys. Chem. Lett.* **3**, 1169–1175 (2012).
16. Akselrod, G. M. et al. Visualization of exciton transport in ordered and disordered molecular solids. *Nat. Commun.* **5**, 4646 (2014).
17. Chuang, C.-H. M. et al. Open-circuit voltage deficit, radiative sub-bandgap states, and prospects in quantum dot solar cells. *Nano Lett.* **15**, 3286–3294 (2015).
18. Blancon, C. Extremely efficient internal exciton dissociation through edge states in layered 2D perovskites. *Science* **355**, 1288–1292 (2017).
19. Congreve, D. N. et al. Tunable light-emitting diodes utilizing quantum-confined layered perovskite emitters. *ACS Photonics* **4**, 476–481 (2017).
20. Zhang, J. et al. Layered ultrathin PbI_2 single crystals for high sensitivity flexible photodetectors. *J. Mater. Chem. C* **3**, 4402–4406 (2015).
21. Derenzo, S. E. et al. Experimental and theoretical studies of donor–acceptor scintillation from PbI_2. *J. Lumin.* **134**, 28–34 (2013).
22. Cooper, J. K., Franco, A. M., Gul, S., Corrado, C. & Zhang, J. Z. Characterization of primary amine capped CdSe, ZnSe, and ZnS quantum dots by FT-IR: determination of surface bonding interaction and identification of selective desorption. *Langmuir* **27**, 8486–8493 (2011).
23. Sayevich, V. et al. Hybrid *N*-butylamine-based ligands for switching the colloidal solubility and regimentation of inorganic-capped nanocrystals. *ACS Nano* **11**, 1559–1571 (2017).
24. Anderson, N. C., Hendricks, M. P., Choi, J. J. & Owen, J. S. Ligand exchange and the stoichiometry of metal chalcogenide nanocrystals: spectroscopic observation of facile metal-carboxylate displacement and binding. *J. Am. Chem. Soc.* **135**, 18536–18548 (2013).
25. Barrit, D. et al. Hybrid perovskite solar cells: in situ investigation of solution-processed PbI_2 reveals metastable precursors and a pathway to producing porous thin films. *J. Mater. Res.* **32**, 1899–1907 (2017).
26. Munir, R. et al. Hybrid perovskite thin-film photovoltaics: in situ diagnostics and importance of the precursor solvate phases. *Adv. Mater.* **29**, 1604113 (2017).
27. Akselrod, G. M. et al. Subdiffusive exciton transport in quantum dot solids. *Nano Lett.* **14**, 3556–3562 (2014).
28. Sandeep, C. S. S. et al. Epitaxially connected PbSe quantum-dot films: controlled neck formation and optoelectronic properties. *ACS Nano* **8**, 11499–11511 (2014).
29. Murray, C. B., Kagan, C. R. & Bawendi, M. G. Synthesis and characterization of monodisperse nanocrystals and close-packed nanocrystal assemblies. *Annu. Rev. Mater. Sci.* **30**, 545–610 (2000).
30. Hanrath, T., Choi, J. J. & Smilgies, D.-M. Structure/processing relationships of highly ordered lead salt nanocrystal superlattices. *ACS Nano* **3**, 2975–2988 (2009).
31. Rolland, A., Richard, J., Kleider, J. P. & Mencaraglia, D. Electrical properties of amorphous silicon transistors and MIS-devices: comparative study of top nitride and bottom nitride configurations. *J. Electrochem. Soc.* **140**, 3679–3683 (1993).
32. Zhitomirsky, D., Voznyy, O., Hoogland, S. & Sargent, E. H. Measuring charge carrier diffusion in coupled colloidal quantum dot solids. *ACS Nano* **7**, 5282–5290 (2013).
33. Choi, J. J. et al. Photogenerated exciton dissociation in highly coupled lead salt nanocrystal assemblies. *Nano Lett.* **10**, 1805–1811 (2010).
34. Makarov, N. S. et al. Spectral and dynamical properties of single excitons, biexcitons, and trions in cesium–lead-halide perovskite quantum dots. *Nano Lett.* **16**, 2349–2362 (2016).
35. Park, Y.-S., Bae, W. K., Pietryga, J. M. & Klimov, V. I. Auger recombination of biexcitons and negative and positive trions in individual quantum dots. *ACS Nano* **8**, 7288–7296 (2014).

Acknowledgements

This publication is based in part on work supported by the Natural Sciences and Engineering Research Council of Canada, by the Ontario Research Fund Research Excellence Program and by Award OSR-2017-CPF-3321-03 made by King Abdullah University of Science and Technology (KAUST). Some of the GIWAXS/GISAXS measurements were performed at the Cornell High Energy Synchrotron Source (CHESS), supported by the NSF Award DMR-1332208. This work also made use of the South Carolina SAXS Collaborative using a SAXSLab Ganesha for the GISAXS/GIWAXS measurements, supported by the NSF Major Research Instrumentation program (award no. DMR-1428620). We thank U. Jeng for the GIWAXS tested at the National Synchrotron Radiation Research Center, Taiwan, China. We thank L. Goncharova for assistance with RBS measurements. We thank D. Kopilovic, E. Palmiano, L. Levina and R. Wolowiec for the technical support.

Author contributions

J.X. conceived the idea and contributed to most experimental work. E.H.S. supervised the project. O.V., A.A. and S.O.K. co-supervised the project. Mengxia Liu assisted in the device fabrication and experiment design. S.H. assisted in the devices certificate and experiment design. A.R.K., M.A. and A.A. performed the in situ measurements of film formation. R.M., M.S., A.S. and R.Q.B. carried out the GISAXS/WAXS measurements. G.W. and M.W. performed the AFM and PL measurements. A.H.P. performed the TA measurements. B.S. carried out the FET measurements. O.V. and O.O. carried out the device simulations. Min Liu carried out microscopic studies. O.V. facilitated the RBS analysis. J.X., O.V. and E.H.S. wrote the manuscript. All the authors assisted in the experiments and provided comments on the text.

Competing interests

The authors declare no competing interests.

Additional information

Supplementary information is available for this paper at https://doi.org/10.1038/s41565-018-0117-z.

Reprints and permissions information is available at www.nature.com/reprints.

Correspondence and requests for materials should be addressed to A.A. or E.H.S.

Methods

Ligand exchange in solution. PbS CQDs (bandgap ~1.3 eV) capped with oleic acid and dispersed in octane (50 mg ml^{-1}) were used. The solution-exchange process was modified from that of our previous report[9]. The precursor solution for ligand exchange was made from lead halides (lead iodide 100 mM and lead bromide 40 mM) in DMF, with ammonium acetate (60 mM) to improve the solubility. The ligand exchange was performed in a centrifuge tube in air. PbS CQD octane solution (2.5 ml, 50 mg ml^{-1}) was first diluted in 10 ml octane and then added to a 20 ml precursor solution in DMF. These were mixed vigorously for ~2 min until the CQDs were totally transferred from the octane phase to the DMF phase. The CQDs in the DMF phase were washed three times using octane and then precipitated by adding toluene (~50–60% in a volume ratio compared with DMF). After centrifugation, the CQDs were separated and then dried in vacuum for 30 min to obtain PbI_2-capped CQD solid powders.

Matrix engineering and film formation. The hybrid amine was prepared by mixing BTA, amylamine and hexylamine (volume ratio 10:3:2). The hybrid amine was used to functionalize the surface of the as-prepared PbI_2-capped CQD solid powder to produce colloidal dispersions (the so-called CQD PV ink) with a large range of concentrations (~170–375 mg ml^{-1}). The CQD PV inks were then spun cast (1,500 revolutions per minute (r.p.m.) for 5 s and then 2,000 r.p.m. for 1 min) to form the initial films of different thickness. The pristine films were glassy and soft. A postannealing at 75 °C for ~15 min in an N_2-filled glovebox was performed to solidify the matrix and densify the CQD films. In control films, BTA or DMF was used to disperse the CQD solid powder to prepare the PV ink. In best-performing BTA films, however, the postannealing step needed to be eliminated as in previous reports. To tune the matrix-to-CQD ratio in the films, additional PbI_2 was dissolved in the solvent (hybrid amine, BTA or DMF) to disperse the CQD solid powder.

CQD planar solar cell fabrication. The ZnO nanoparticle dispersion in methanol and chloroform (1:1 by volume ratio) was spun cast on ITO to form an electron-transport layer (ETL) (~100–150 nm in thickness). The ZnO nanoparticles were synthesized following a published recipe[8]. The CQD active absorber (~250–600 nm in thickness) was deposited on the ZnO layer using the fresh PV ink followed by a postannealing step as described above. Then the hole-transport layer (HTL) (~50 nm in thickness) was two layers of PbS CQD ligand exchanged by 1,2-ethanedithiol (EDT) (0.01 vol% in acetonitrile). In each layer, CQDs capped with oleic acid (50 mg ml^{-1}) were spun cast, followed by a 30 s soaking in diluted EDT (0.01 vol% in acetonitrile) and three washings with acetonitrile. Finally, a top contact of 100 nm of gold was deposited through a shadow mask under a vacuum of 10^{-7} Torr.

AM 1.5G solar efficiency measurement. The active area (0.049 cm^2) was determined by the aperture placed between the solar cell and the AM1.5G solar simulator (Sciencetech class A). Through this aperture, the light intensity (1 sun, 100 mW cm^{-2}) was calibrated using a Melles–Griot broadband power meter. The spectral mismatch was calibrated using a reference solar cell (Newport). The *J*–*V* curve was measured by a Keithley multimeter by scanning the bias forward (–0.7 V to 0.1 V) and backward (0.1 V to –0.7 V) to estimate the hysteresis effect. The steady-state PCE was then measured by fixing the bias at the maximum power output point determined from *J*–*V* curves (Supplementary Fig. 24).

RBS. RBS measurements were performed at the Tandetron facility at the University of Western Ontario. CQD films of ~300 nm thickness were deposited on Si substrates to avoid overlaps with the main elements in CQD films. All the samples were measured with a 3.7 MeV He^{++} beam (non-Rutherford resonance for nitrogen) and a dose of 10 μC.

GISAXS and GIWAXS. GISAXS was carried out at the Cornell High Energy Synchrotron Source. The wavelength of the X-ray beam was 1.17 Å. A wide band-pass (1.47%) double-bounce multilayer monochromator was employed. The incident angle was set to 0.5° with respect to the sample plane. The exposure time was 3 s. GISAXS and GIWAXS were also conducted using a SAXSLab Ganesha at the South Carolina SAXS Collaborative. A Xenocs GeniX 3D microfocus source was used with a copper target to produce monochromatic beam with a 0.154 nm wavelength. The instrument was calibrated just prior to the measurement using National Instrument of Standard and Technology reference material 640c. A Pilatus 300K detector (Dectris) was used to collect the 2D scattering pattern with a nominal pixel dimension of 172 × 172 μm. GISAXS data were acquired with an incident X-ray angle (α_i) of 0.5° with respect to the substrate using an X-ray flux of ~21.4 M photons per second upon the samples. Likewise, GIWAXS data were collected with $\alpha_i = 2°$ and an X-ray flux of ~36.3 M photon per second. The sample-to-detector distance was maintained at 452.1 and 112.1 mm for GISAXS and GIWAXS measurements, respectively.

Long-time TA (flash photolysis). Pump pulses were generated with a regenerative amplified ytterbium:potassium–gadolinium–tungstate laser at a 5 kHz repetition rate (PHAROS (Light Conversion)). The 1,030 nm fundamental was sent through an optical parametric amplifier (OrpheusLight Conversion)), and the second harmonic of the idler was chosen for the 750 nm pump pulse. The probe was generated by a continuous-wave 1,310 nm laser diode (LPM1310-05E (Newport)). Both beams were focused onto the sample, and the probe was coupled to an InGaAs-amplified detector (PDA10D (Thorlabs)). The lifetime response was measured using a 1 GHz oscilloscope (DSO8104A (Agilent)), which was triggered by the pump laser.

AFM. The AFM study was done with an Asylum Research Cypher AFM equipped with AC240TM-R3 probes (resonant frequency 70 kHz, spring constant 2 N m^{-1}). Nanomechanical force spectroscopy was conducted with a trigger indentation force of 8 nN loaded at a rate of 2 μm s^{-1}. Topographic imaging was performed in the tapping mode.

Other characterizations. Fourier transform infrared spectroscopy (FTIR) measurements were done using a Bruker Vertex 80 (4,000 to 600 cm^{-1}, resolution 4 cm^{-1}) in the top configuration (attenuated total reflection (ATR)). Steady-state PL was carried out using an HORIBA Fluorolog-3 spectrofluorometer equipped with UV–vis–NIR photomultiplier tube detectors and a monochromatized xenon lamp excitation. UV–vis–infrared absorption was carried out on a PerkinElmer LAMBDA 950 spectrophotometer. EQE spectra measurements were carried out following a previously published processes[4].

Reporting Summary. Further information on experimental design is available in the Nature Research Reporting Summary linked to this article.

Data availability. The authors declare that the data supporting the findings of this study are available within the paper and its supplementary information files. The data that support the findings of this study are also available from the corresponding authors upon reasonable request.

nature research

Corresponding author(s): Edward H. Sargent

Solar Cells Reporting Summary

Nature Research wishes to improve the reproducibility of the work that we publish. This form is intended for publication with all accepted papers reporting the characterization of photovoltaic devices and provides structure for consistency and transparency in reporting. Some list items might not apply to an individual manuscript, but all fields must be completed for clarity.

For further information on Nature Research policies, including our data availability policy, see Authors & Referees.

Experimental design

Please check: are the following details reported in the manuscript?

1. Dimensions

Area of the tested solar cells	☒ Yes ☐ No	Certified device with small area ~0.049cm^2 (Supplementary Figure S21). Large-area device 1cm^2 (Supplementary Figure S22).
Method used to determine the device area	☒ Yes ☐ No	See the Methods (AM1.5 solar efficiency measurement). Optical aperture is used to define the active area.

2. Current-voltage characterization

Current density-voltage (J-V) plots in both forward and backward direction	☒ Yes ☐ No	See Methods (AM1.5 solar efficiency measurement) and Supplementary Figure S24.
Voltage scan conditions *For instance: scan direction, speed, dwell times*	☒ Yes ☐ No	See Methods (AM1.5 solar efficiency measurement) and Supplementary Figure S24. Forward scanning (-0.7 V to 0.1 V) and backward (0.1 V to -0.7 V) with different speeds. No hysteresis was observed in all typies of CQD PV devices. Steady-state power conversion efficiency (PCE) is then measured by fixing the bias at the maximum power output point (VMPP).The PCE reported in main text was determined by the steady-state performance.
Test environment *For instance: characterization temperature, in air or in glove box*	☒ Yes ☐ No	NEWPORT certificate tested in N2. Temperature 25C.
Protocol for preconditioning of the device before its characterization	☒ Yes ☐ No	See Methods (AM1.5 solar efficiency measurement) and Supplementary Figure S24.
Stability of the J-V characteristic *Verified with time evolution of the maximum power point or with the photocurrent at maximum power point; see ref. 7 for details.*	☒ Yes ☐ No	See Methods (AM1.5 solar efficiency measurement) and Supplementary Figure S24. Steady-state power conversion efficiency (PCE) is measured by fixing the bias at the maximum power output point (VMPP).The PCE reported in main text is determined by steady-state performance at maximum power point (MPP). Because there is no hysteresis in all CQD PVs, the PCE value from steady-state tests and J-V curves are identical.

3. Hysteresis or any other unusual behaviour

Description of the unusual behaviour observed during the characterization	☒ Yes ☐ No	See Methods (AM1.5 solar efficiency measurement) and Supplementary Figure S24. No hysteresis was observed for all CQD PV devices, including both the control devices and hybrid-amine devices. The hysteresis-free behavior in CQD PVs is also widely-accepted in literature.
Related experimental data	☒ Yes ☐ No	Supplementary Figure S24.

4. Efficiency

External quantum efficiency (EQE) or incident photons to current efficiency (IPCE)	☒ Yes ☐ No	Figure 5 and Supplementary Figure S22.
A comparison between the integrated response under the standard reference spectrum and the response measure under the simulator	☒ Yes ☐ No	Figure 5 and Supplementary Figure S22.
For tandem solar cells, the bias illumination and bias voltage used for each subcell	☐ Yes ☒ No	Not applicable. No tandem device was involved in this work.

5. Calibration

Light source and reference cell or sensor used for the characterization	☒ Yes ☐ No	See Methods (AM1.5 solar efficiency measurement)
Confirmation that the reference cell was calibrated and certified	☒ Yes ☐ No	See Methods (AM1.5 solar efficiency measurement)
Calculation of spectral mismatch between the reference cell and the devices under test	☒ Yes ☐ No	See Methods (AM1.5 solar efficiency measurement)

6. Mask/aperture

Size of the mask/aperture used during testing	☒ Yes ☐ No	See Methods (AM1.5 solar efficiency measurement) and Supplementary Figure S21. Aperture size 0.049cm^2 for small-area device. Aperture size 1cm^2 for large-area device.
Variation of the measured short-circuit current density with the mask/aperture area	☒ Yes ☐ No	See Methods (AM1.5 solar efficiency measurement) and Supplementary Figure S21. Tested with aperture between solar source and device.

7. Performance certification

Identity of the independent certification laboratory that confirmed the photovoltaic performance	☒ Yes ☐ No	Supplementary Figure S21. Certificate Performance from NEWPORT agrees with the value tested in our lab (Fig 5).
A copy of any certificate(s) *Provide in Supplementary Information*	☒ Yes ☐ No	Supplementary Figure S21.

8. Statistics

Number of solar cells tested	☒ Yes ☐ No	Fig 5. In the thickness-dependent studies, for each thickness, 12 samples for each type (control and hybrid) fabricated in the same batch were tested.
Statistical analysis of the device performance	☒ Yes ☐ No	Fig 5. The agreement between the certified value and that tested in lab verifies the reproducibility and stability of our devices.

9. Long-term stability analysis

Type of analysis, bias conditions and environmental conditions *For instance: illumination type, temperature, atmosphere humidity, encapsulation method, preconditioning temperature*	☐ Yes ☒ No	As widely reported in the literature (see below references), the state-of-art CQD devices show no hysteresis and are stable in air. We found our devices are consistently hysteresis-free and air-stable, very similar with that reported for control devices. Ref 1. Chuang, C.-H. M., Brown, P. R., Bulović, V. & Bawendi, M. G. Improved performance and stability in quantum dot solar cells through band alignment engineering. Nat Mater 13, 796–801 (2014). Ref 2. Liu, M. et al. Hybrid organic-inorganic inks flatten the energy landscape in colloidal quantum dot solids. Nat Mater 16, 258–263 (2016).